RESEARCH ARTICLE | OCTOBER 18 2023

Theoretical and numerical analysis of the flow through a diffuser/nozzle element in pulsatile laminar conditions ⊘

Paolo Peruzzo ✉ iD

Check for updates

CrossMark

View Online   Export Citation

Articles You May Be Interested In

Completing the dark matter solutions in degenerate Kaluza-Klein theory

J. Math. Phys. (April 2019)

Gibbs measures based on 1d (an)harmonic oscillators as mean-field limits

J. Math. Phys. (April 2018)

An upper diameter bound for compact Ricci solitons with application to the Hitchin–Thorpe inequality. II

J. Math. Phys. (April 2018)

Theoretical and numerical analysis of the flow through a diffuser/nozzle element in pulsatile laminar conditions

Paolo Peruzzo[a] [iD]

AFFILIATIONS

Cardiovascular Fluid Dynamics Laboratory HER, Department of Civil, Environmental and Architectural Engineering,
University of Padova, Italy

[a]Author to whom correspondence should be addressed: paolo.peruzzo@dicea.unipd.it

ABSTRACT

Diffuser/nozzle pipes produce a directional flow resistance that is often exploited in microcirculation to generate a pumping action. This work presents an approximate time-dependent theoretical solution based on the mechanical energy conservation equation to predict the laminar flow rate through an ideal diffuser/nozzle pump. The theoretical solution is then used to characterize the dimensionless parameters that control the dynamics of the valveless pump in the pulsatile flow regime. A suitable numerical model is also implemented to solve the flow in a parametrized two-dimensional axial-symmetric domain subjected to an oscillating pressure, and its results are used to assess the theoretical solution. The pump dynamics and the main model parameters, such as the energy-loss coefficients, result in the following dependence on the ratios between the viscous force, the advective inertia, and the temporal inertia, i.e., the Reynolds (Re_d), Womersley (Wo_d), and Strouhal (St) numbers referred to throat diameter. In particular, The Womersley number plays an essential role in controlling the global energy loss when $Re_d < 100$. The flow transition is also investigated and found when Re_d exceeds a critical value, which increases with Wo_d. Finally, the pump efficiency is found to reach its maximum when the convective and temporal inertia become comparable, i.e., $St = O(1)$, consistent with the observed range of St in real-world diffuser/nozzle pumps. This optimum range of functioning of the pump is also observed for cerebrospinal pulsatile flow in the Sylvius aqueduct, suggesting that the modeled mechanism is used to promote or enhance cerebrospinal fluid circulation.

I. INTRODUCTION

Several fluidic applications of mechanical engineering, medicine, and chemistry use microcirculation flow systems.[1] The development of microelectromechanical systems (MEMs) has encouraged the widespread of micropumps and, more recently, their application to drug delivery in the medical field.[2,3] Moreover, pulsatile microcirculation is observed in biological systems; physiological processes, such as oxygen transport into the fetuses cardiovascular apparatus, or cerebrospinal fluid circulation, occur indeed also at the microscale.[4–10]

Circulation systems, either biological or man-made, are typically designed to avoid local backward flows; however, check valves, commonly adopted in engineering applications to intercept undesired backward flow, often do not work efficiently at small scales. Therefore, in the mechanical design of microsystems, different solutions are exploited to guarantee the one-directional flow under pumping conditions.[11] Pulsatile microcirculation often uses hydraulic principles based on the asymmetry of either the impedance, the so-called Libeau

effect,[12–15] or the shape of some elements according to the direction of the flow.[16–18] In the latter case, the pump that feeds the circuit includes one, or more than one, diffuser/nozzle elements that force the flow toward a preferential direction.[19,20] In this type of pump (Fig. 1), pulsatile overpressure is typically transmitted by an actuator into a chamber, which cyclically empties (pump mode) and fills (supply mode). Consequently, the fluid flows in the diverging-wall (diffuser) and converging-wall (nozzle) direction, alternatively. Flow resistance along the diffuser direction is typically lower than that experienced in the opposite direction, resulting in a flow that, on average, prevails in the diffuser verse.

The literature reports many studies that focus on optimizing the diffuser/nozzle geometry. These studies investigate the role of pipe geometry in energy dissipation at different hydraulic regimes through experimental and numerical approaches.[21–25] The pipe shape primarily controls the difference in flow rate between the diverging and converging flow modes and then the pump efficiency.[26] In particular, tapering/
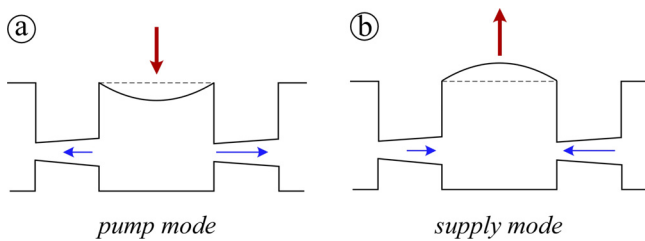
18 October 2023 13:51:10

FIG. 1. Schematic of a diffuser/nozzle pump driven by an oscillating pressure: pump mode (a) and supply mode (b). Red arrows indicate the pressure solicitation; blue arrows indicate the resulting flow rate (arrow length indicates the flow intensity). Adapted from Ref. 7.

sharpening the inlet reduces/increases pressure loss. Moreover, the pump efficiency increases when the angle of the cone increases to an optimum value that ranges between 5° and 10°, depending on the geometry of the diffuser.[27,28]

Most of these studies aimed at characterizing a specific device. Only a few works propose a general framework for the micropumps dynamics developing closed-form solutions to estimate the flow rate.[29–31] In particular, many efforts have been devoted to estimating the maximum volume flux through the nozzle/diffuser by using lumped-mass models or strongly simplified pump dynamics.[19,32,33]

A more accurate model considering fluid inertia has been developed by Eames, Azarbadegan, and Zangeneh,[34] who found that the average flow rate is proportional to the external pressure drop; however, the role of temporal inertia remains generally elusive. Indeed, the criteria adopted in the literature to design micropumps often assume quasi-steady flow conditions.[22,26,27] Nevertheless, the temporal flow acceleration likely contrasts the laminar to turbulent transition within a pipe, influences the velocity profile, and, hence energy losses. Therefore, the results provided by the current literature should be used with some caution since the temporal acceleration may strongly affect the pump dynamics.

This work aims to bridge this knowledge gap and clarify the role of temporal inertia on the flow regime transition within diffuser/nozzle elements and on energy losses.

For this purpose, the phenomenology of the oscillating flow through a diffuser/nozzle is first described, highlighting the different flow features and regimes. Second, a theoretical solution of the 1D incompressible Newtonian flow equation is proposed to model the

laminar flow through a nozzle/diffuser element under idealized oscillating pressure forcing. Third, the solution is used to estimate the dimensionless parameters that control the dynamics of the valveless pump in the pulsatile flow regime. Finally, a suitable numerical model describing the above flow is implemented and its results are compared with the theoretical predictions. This comparison allowed one to: (i) assess the capability of the theoretical solution to describe the oscillating flow rate of the pump; (ii) determine the condition for pulsatile flows to be laminar; (iii) unravel the dependence of the model parameters on the fundamental dimensionless groups, and (iv) find the conditions for the optimum pump performance.

II. DIFFUSER/NOZZLE HYDRODYNAMICS

In the literature, an organic and coherent treatment of the fluid dynamic is limited to the steady flow within a diffuser.[35] For this reason, in this section, a preliminary numerical analysis of the pump dynamics subjected to an oscillating flow is presented with the intent of helping the reader to approach the problem.

To illustrate the hydrodynamics of a valveless pump, a series of large eddy simulations (LES) with a Smagorinsky subfilter model is performed. A three-dimensional (3D) conical diffuser/nozzle element is solicited by a pressure gradient between two chambers according to the scheme shown in Fig. 2(a), in which flows water with density $\rho = 1000 \, \text{kg/m}^3$ and dynamic viscosity $\mu = 0.001 \, \text{Pa s}$. Specifically, the duct has a length $L = 10 \, \text{mm}$ and the minimum and maximum diameter $d = 0.75 \, \text{mm}$ and $D = 2.0 \, \text{mm}$, respectively, resulting in a cone angle $\theta = 7.2°$; the chambers have a radius $a = 10 \, \text{mm}$. Overall, the model grid consisted of 940 000 tetrahedral elements, indicatively.

The difference between pressure p_1 and p_2 in the two chambers periodically changes over time as

$$p_1(t) - p_2(t) = p_0 \, \sin(\omega t), \tag{1}$$

where p_0 is the maximum pressure difference across the duct, ω is the angular frequency, and t is the time. The flow rate, Q, is positive when the pump works in the diffuser mode, whereas it is negative in the nozzle mode [Fig. 2(b)].

The hydrodynamics through the duct shows different regimes and flow patterns according to the pumping frequency, f (or period $T = 1/f$), as shown in the three exemplifying cases of Fig. 3, in which $p_1 = p_0 \, \sin(\omega t)$ and $p_2 = 0$ Pa, with $p_0 = 5.0$ kPa.

At a frequency of 1 Hz [panel (a)], the flow pattern in the diffuser modality reveals bistable stall regions that can switch from one side of
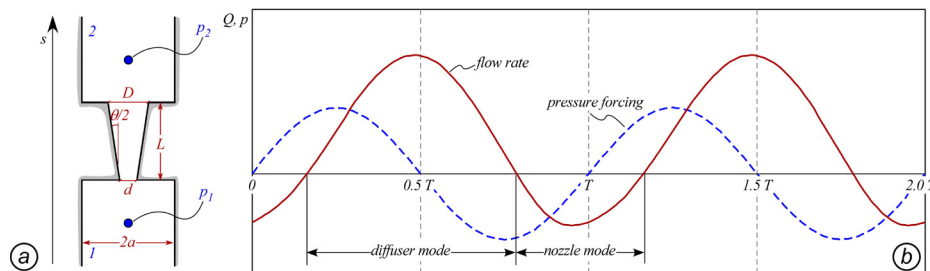
FIG. 2. Sketch of the diffuser/nozzle model. (a) Geometry of the valveless pump consisting of a diffuser/nozzle element of length L connecting chambers 1 and 2 whose pressure is p_1 and p_2; D and d are the largest and smallest diameter of the diffuser/nozzle element, respectively, and θ is the cone angle. (b) Temporal distribution of the pressure forcing, p, (blue dashed line) and volume flux, Q, through the diffuser/nozzle (solid red line). The volume flux is expected to be higher in the diffuser direction than in the nozzle direction.

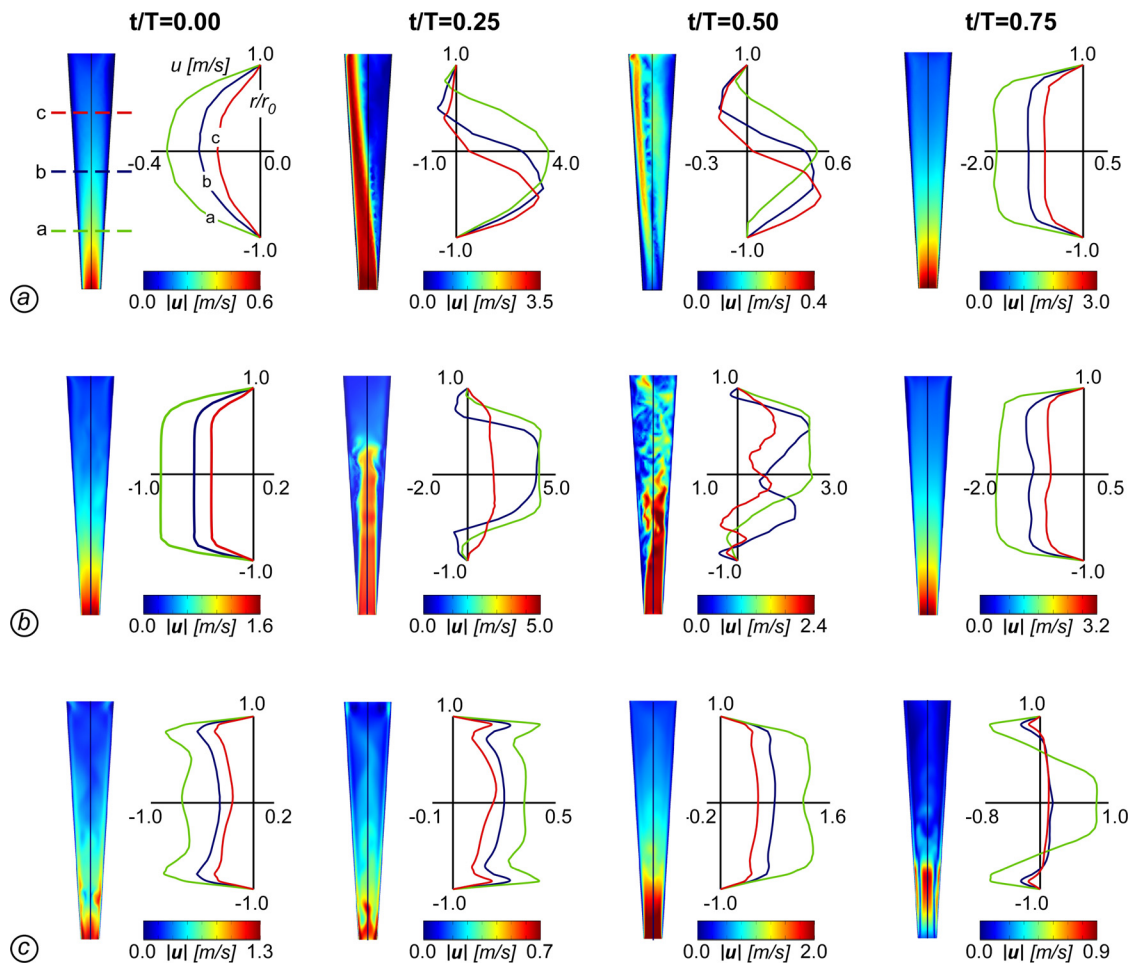**FIG. 3.** Velocity magnitude, $|\mathbf{u}|$, within a diffuser/nozzle with L = 10 mm, d = 0.75 mm, and D = 2.0 mm 2 in four instants of time ($t/T = 0$, 0.25, 0.5, and 0.75) and corresponding axial velocity, u, distributions in three characteristics sections placed at $L/4$, $L/2$, and $3L/4$ for (a) $f = 1$ Hz, (b) $f = 20$ Hz, and (c) $f = 100$ Hz. The profile in the radial direction, r, is normalized by the local radius of the pipe, r_0. The pressure amplitude is $p_0 = 5$ kPa in the three cases.

the pipe to the other, as seen in steady flow.[35] This creates velocity profiles within the duct that display both positive and negative velocities. However, in the nozzle modality, we do not observe any flow separation. When we increase the frequency to 20 Hz [panel (b)], the flow displays a central high-velocity region with non-symmetric profiles during the diffuser modality, but the velocity profiles in the nozzle modality remain largely unchanged. Finally, at a frequency of 100 Hz [panel (c)], the flow pattern remains constant in the time series analysis. We observe a small stable backflow region that exists for a short period of the diffuser modality. In this case, the velocity profiles are self-similar along the duct, indicating a different response to the oscillatory pressure in the bulk region and near the wall.

In microfluidics, to define the hydraulic regime within the pump, the comparison of the characteristic Reynolds number (Re_d estimated in the throat of the diffuser in this problem) with the transitional value of 2000–2300 is often ineffective. Specifically, in steady flows when the ducts are relatively short ($1 < L/d < 70$), one can distinguish the flow regime by introducing the critical Reynolds number $Re_{c0} = 30L/d$.[1,26]

For $Re_d < Re_{c0}$, the flow is dominated by the viscous loss, and the regime is laminar. On the other hand, for $Re_d > Re_{c0}$, the flow is driven by the inertia; however, the regime cannot be said turbulent as the duct is shorter than the entrance length needed to fully develop the turbulence.

The criterion illustrated can be extended in pulsatile flows only when the frequency, f, is low enough that the flow can be treated as quasi-steady [e.g., Fig. 3(a)].[36] In this case, $Re_d > Re_{c0}$ at the velocity peak, and the velocity field is not stable in the diffuser modality. Inconsistent with reality, the Smagorinsky model results in non-zero eddy viscosity, ν_t, even when the flow is fully resolved. In the current analysis, the value of ν_t is approximately 10^{-6} m²/s in the vicinity of the wall of the diffuser throat and ranges from 10^{-9} to 10^{-7} m²/s in the bulk flow region. These values are relatively small and do not seem representative of actual turbulent processes. At higher frequencies, the temporal acceleration is expected to broaden the laminar regime similarly to the laminar-turbulent transition observed in long pipes with constant diameter.[37] The flow condition of panel (c) seems to confirm

this hypothesis. In this case, the model estimated a value at the velocity peak higher than the threshold limit of steady flow ($Re_d > Re_{c0}$). Nevertheless, the velocity profiles are self-similar and kept regular in time, suggesting that the regime is still laminar. Clearly, the relation proposed to determine the regime transition for long pipes cannot be straightforwardly extended to short channels with variable diameters treated here.

In any case, these preliminary numerical experiments prefigure that the transition of an oscillatory flow through a diffuser is not exclusively led by the comparison between advective inertia and viscous force, i.e., by the Reynolds number, but also by the ratios of these two terms with the temporal inertia, which are expressed through the Strouhal and Womersley number, respectively.

In Secs. V A, these three parameters are analyzed to assess the transition condition into a diffuser/nozzle pump. For this purpose, we exploit the property of regularity and self-similarity of the velocity profile in the laminar regime that lends to being represented through a two-dimensional (2D) axial-symmetric scheme. Using a 2D model has significantly reduced the computational costs and allowed one to carry out several numerical experiments, which were used to frame the problem. The proper definition of the laminar regime is fundamental in the diffuser/nozzle pump design because, as we will see in Sec. V C, the maximum performances are achieved in this regime.

III. THEORY

A. The 1D model

The laminar flow in a diffuser/nozzle pipe illustrated in Fig. 3(c) can be described according to a one-dimensional (1D) model, provided that the degree of divergence of the pipe walls is small, such that radial velocity is significantly smaller than the axial one.

In this setting, the pump dynamics can be described by assuming the mechanical energy conservation equation for an incompressible Newtonian fluid, which reads (see Appendix A)

$$\frac{\partial H(s,t)}{\partial s} = -\frac{\beta(t)}{g}\frac{\partial U(s,t)}{\partial t} - j(s,t), \qquad (2)$$

where $H = p/\gamma + \alpha U^2/2g$ is the mechanical energy of the fluid per unit weight (hereinafter denoted simply as energy or total head), U is the cross-sectional average velocity, α and β the correction factors, g the gravity acceleration, γ the specific gravity, and j the internal head loss per unit length. The model is based on the following assumptions:

(1) the cross sections of the chambers are significantly larger than the pipe cross section, so that the flow velocity within the two chambers can be neglected, and the total head is essentially due to the pressure;
(2) the wall of the pipe is rigid and then the cross-sectional area of the diffuser/nozzle depends only on s;
(3) the velocity profiles are almost self-similar along the pipe, consequently the correction factors depend only on t, i.e., $\alpha(s,t) \approx \alpha(t)$ and $\beta(s,t) \approx \beta(t)$;
(4) the energy loss can be related to the mean flow velocity of the narrowest section of the diffuser/nozzle, according to the definition provided by the literature within a diffuser/nozzle channel.[22,27]

With these assumptions, a quasi-linear differential equation of the volume flow rate, Q, in the pipe can be obtained by integrating Eq. (2) between the two chambers (see Appendix B)

$$\frac{p_0}{\gamma}\sin(\omega t) = \frac{\beta(t)}{g}\frac{4L}{\pi dD}\frac{dQ(t)}{dt} + \frac{\zeta(t)}{g}\frac{2\nu}{\pi d^3}Q(t). \qquad (3)$$

Here, ν is the kinematic viscosity and ζ is a coefficient that controls the overall energy loss due to friction and possible flow separation.

The parameter ζ depends on the flow direction, and it is significantly different when the pipe operates as a diffuser or a nozzle. Q is defined as positive in the diffuser mode, hence for the parameter ζ, as well as for all parameters that depend on ζ, the subscript "$\pm$" is starting now used to denote the diffuser (subscript +) and nozzle modes (subscript –).

Equation (3) is rewritten as

$$\frac{dQ(t)}{dt} + \psi_{\pm}(t)Q(t) - Q_0\frac{\omega}{\beta(t)}\sin(\omega t) = 0 \qquad (4)$$

with

$$Q_0 = \frac{p_0}{\rho\omega}\frac{\pi dD}{4L} \qquad (5)$$

the characteristic flow rate of the problem and

$$\psi_{\pm}(t) = \frac{\zeta_{\pm}(t)}{\beta(t)}\frac{\nu D}{2Ld^2} \qquad (6)$$

two characteristic frequencies that depend on the tube shape and the energy dissipation.

B. Model parameters

Before proposing a closed-form solution of Eq. (4), a brief analysis of the parameters is helpful to explore the results of the theoretical model. Equation (3) describes the flow dynamics through the diffuser/nozzle element. The term on the left-hand side is the forcing factor, while the first and second on the right-hand side are associated with temporal inertia and energy loss, respectively.

To evaluate the relative importance of each term, we introduce two geometrical, one temporal, and one kinematic scale quantities. Specifically, d and L are the two fundamental lengths of the problem. The temporal scale of the problem is related to the forcing pressure period $1/\omega$, whereas the intensity of the flow can be quantified by means of the velocity U_0. The latter is calculated in the pipe throat for the characteristic flow rate Q_0 of Eq. (5), and it is defined as

$$U_0 = \frac{4Q_0}{\pi d^2}. \qquad (7)$$

We can then introduce the dimensionless time $\tilde{t}$, the dimensionless volume flux $\tilde{Q}$, and the dimensionless pressure $\tilde{p}$ as $\tilde{t} = \omega t$, $\tilde{Q} = Q/(U_0 d^2)$, and $\tilde{p} = p_0/(\rho U_0^2)$. Consequently, the dimensionless form of Eq. (3) reads

$$\underbrace{\tilde{p}\sin(\tilde{t})}_{forcing\ term} = \underbrace{\frac{4}{\pi}\frac{d}{D}\beta St\frac{d\tilde{Q}}{d\tilde{t}}}_{inertia} + \underbrace{\frac{2}{\pi}\frac{\zeta_{\pm}}{Re_d}\tilde{Q}}_{viscous\ force}. \qquad (8)$$

Here, $St = \omega L/U_0$ is the Strouhal number and $Re_d = (U_0 d)/\nu$ is the throat Reynolds number.

Alternatively, St can be expressed as

$$St = 4\frac{L}{d}\frac{Wo_d^2}{Re_d}, \qquad (9)$$

where $Wo_d = d\sqrt{\omega/4\nu}$ is the Womersley number referred to d.

According to Eqs. (8) and (9), the flow rate through a diffuser/nozzle pipe depends on two of the three dimensionless numbers St, Re_d, and Wo_d, which express, respectively, the ratio between *i*) temporal and convective inertia, *ii*) convective inertia and viscous force, and *iii*) temporal inertia and viscous force. In the present work, the working of the diffuser/nozzle pump is investigated as a function of these dimensionless numbers (Sec. V).

Furthermore, the dimensional analysis shows that the pump also depends on two geometric parameters, namely, the slenderness of the pipe, L/d, and the ratio of the diameters d/D. Nevertheless, it is convenient to replace the latter parameter with $\tan \theta$, being $\theta = 2\arctan[(D - d)/L]$.

C. Closed form solutions

A straightforward solution of Eq. (4) can be obtained after replacing $\zeta_+(t)$, $\zeta(t)$, and $\beta(t)$ with three time-independent calibration factors, $\bar{\zeta}_+$, $\bar{\zeta}_-$, and $\bar{\beta}$, which depend on the Reynolds and Womersely number. This simplification allows one to obtain a closed-form solution of Eq. (4) that, as discussed below, still provides a fairly accurate description of the flow. With this simplification, Eq. (4) reduces to the following linear ordinary differential equation:

$$\frac{dQ(t)}{dt} + \psi_\pm Q(t) - \omega\frac{Q_0}{\bar{\beta}}\sin(\omega t) = 0, \qquad (10)$$

with

$$\psi_\pm = \frac{\bar{\zeta}_\pm}{\bar{\beta}}\frac{\nu D}{2Ld^2}. \qquad (11)$$

Furthermore, it is convenient to rewrite the two frequencies $\psi_\pm$ as $\psi_+ = \psi - \Delta\psi$ and $\psi_- = \psi + \Delta\psi$, with $\psi = (\psi_+ + \psi_-)/2$ and $\Delta\psi = (\psi_- - \psi_+)/2$. With this, Eq. (4) reads

$$\frac{dQ(t)}{dt} + \psi Q(t) - \Delta\psi|Q(t)| - \omega\frac{Q_0}{\bar{\beta}}\sin(\omega t) = 0. \qquad (12)$$

Here, the prevailing flow rate in the diffuser verse is due to the term $\Delta\psi|Q(t)|$. This viscous contribution can be approximately treated as a constant during the pumping cycle and related to an equivalent positive volume flux. Consequently, in Eq. (12), we can replace $|Q(t)|$ with a time-independent flow rate, $\varepsilon Q_0/\bar{\beta}$, being $\varepsilon \lesssim 1$ a suitable calibration coefficient. With this, Eq. (12) reads

$$\frac{dQ(t)}{dt} + \psi Q(t) = \varepsilon\Delta\psi\frac{Q_0}{\bar{\beta}} + \omega\frac{Q_0}{\bar{\beta}}\sin(\omega t). \qquad (13)$$

The general solution of this equation reads

$$Q(t) = Ce^{-\psi t} + \varepsilon\frac{\Delta\psi}{\psi}\frac{Q_0}{\bar{\beta}} + \frac{\omega Q_0}{\bar{\beta}(\psi^2 + \omega^2)}[\psi\sin(\omega t) - \omega\cos(\omega t)], \qquad (14)$$

where C is an integration constant.

In the present analysis, the first term in the right-hand side of Eq. (14) can be neglected, as it describes the transition to the equilibrium and vanishes exponentially in time, with timescale $1/\psi$. Both the amplitude and the phase of the flow are affected by the frequencies ω and ψ; thereby in the analysis of the pump dynamics, the dominance of one term to the other can be measured by the ratio $\sigma = \psi/\omega$.

The steady periodic flow in the valveless pump is characterized by a volumetric flux described by the relation

$$Q(t) = \varepsilon\frac{\Delta\bar{\zeta}}{\bar{\zeta}}\frac{Q_0}{\bar{\beta}} + \frac{Q_0}{\bar{\beta}\sqrt{1+\sigma^2}}\sin(\omega t - \varphi), \qquad (15)$$

here $\varphi = \tan^{-1}(1/\sigma)$ and the ratio $\Delta\psi/\psi$ is replaced with $\Delta\bar{\zeta}/\bar{\zeta}$, where $\bar{\zeta} = (\bar{\zeta}_+ + \bar{\zeta}_-)/2$ and $\Delta\bar{\zeta} = (\bar{\zeta}_- - \bar{\zeta}_+)/2$.

The flow is the sum of an oscillating component of amplitude $Q_0/\bar{\beta}\sqrt{(1+\sigma^2)}$ and a steady component in the diffuser direction, due to the asymmetry of the geometry, which depends on the ratio $\Delta\bar{\zeta}/\bar{\zeta}$. The average pump flow rate, hereinafter denoted as Q_{net}, is then given by the first term on right-hand side of Eq. (15).

The dimensional analysis (Sec. III B) suggests that the diffuser/nozzle pump has two limit work conditions. The first is when the viscous term is negligibly small, i.e., when $Re_d \gg 1$ and $Wo_d \gg 1$. In this case the governing Eq. (3) reduces to

$$\frac{p_0}{\gamma}\sin(\omega t) = \frac{\beta}{g}\frac{4L}{\pi dD}\frac{dQ}{dt} \qquad (16)$$

and its solution yields

$$Q(t) = \frac{Q_0}{\bar{\beta}}\sin\left(\omega t - \frac{\pi}{2}\right). \qquad (17)$$

In the second case, the inertial term is negligibly small, i.e., when $Re_d \ll 1$ and $Wo_d \ll 1$, and the governing Eq. (3) reduces to

$$\frac{p_0}{\gamma}\sin(\omega t) = \frac{\zeta}{g}\frac{2\nu}{\pi d^3}Q, \qquad (18)$$

whose solution reads

$$Q(t) = \frac{Q_0}{\bar{\beta}\sigma}\sin(\omega t). \qquad (19)$$

D. Pump efficiency

The efficiency of the pump, η, is defined as

$$\eta = \frac{V_+ - V_-}{V_+ + V_-}, \qquad (20)$$

where V_+ and V_- are the total volumes flowing, respectively, in the diffuser and nozzle direction during one pumping cycle. A value of η equal to 0 means null net flux, on the contrary, $\eta = \pm 1$ indicates that the fluid flows in only one direction.

The limit conditions of the diffuser/nozzle pump given by Eqs. (17) and (19) deserve careful analysis. In both cases, the net flux is null, and the efficiency, η, is equal to 0. It should be noted that, in Eq. (17), $Q(t)$ is in quadrature phase with the forcing pressure, i.e., $\varphi = \pi/2$, and thus $\sigma \rightarrow 0$, being $\tan\varphi = 1/\sigma$. On the contrary, in the second case reported in Eq. (19), the external pressure, $p_0\sin(\omega t)$, and the flow rate, Q, are in phase so that $\varphi = 0$, resulting in $\sigma \rightarrow \infty$.
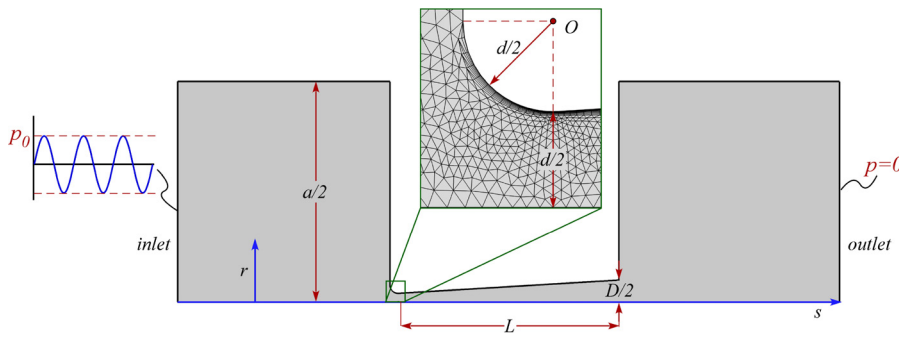
FIG. 4. Sketch of the geometry and boundary conditions used in the CFD simulations. An example of the numerical grid is reported in the zoom (green box). The throat of the diffuser/nozzle element is tapered with a fillet of radius equal to $d/2$.

The limits of Eq. (20) in the space $\sigma \in (0, \infty)$ are then 0. Hence, an operating condition that maximizes η must exist. The present analysis suggests that such a maximum condition should be intermediate between the two limit cases reported in Eqs. (17) and (19), i.e., when the phase φ is far from the values of 0 and $\pi/2$. This means the maximum is achieved when $\tan \varphi$ is equal to

$$\tan \varphi = \frac{1}{\sigma} = \frac{\omega}{\psi} = \kappa, \tag{21}$$

where κ is a $O(1) - O(10)$ coefficient. By replacing Eq. (6) into Eq. (21), and recalling that $St = \omega L/U_0$ with U_0 given by Eqs. (5) and (7), the optimal efficiency is reached when

$$St = \frac{\kappa}{2} \, \bar{\zeta} \, \frac{L}{d} \, \frac{\mu \, \omega_{max}}{p_{0,max}} \tag{22}$$

with ω_{max} and $p_{0,max}$, respectively, the pair of pulsatility and pressure that maximize the efficiency.

IV. NUMERICAL SIMULATIONS

To assess the robustness of the proposed theoretical framework, the flow through a diffuser/nozzle pump has been computed numerically. The hydrodynamics has been solved in a parametrized 2D axisymmetric domain subjected to an oscillating pressure. The numerical model has been implemented in the computational fluid dynamics (CFD) module of COMSOL Multiphysics 5.5 (Comsol, Inc., Stockholm). The software adopted a backward differentiation formulation to solve implicitly the Navier–Stokes equations. The laminar flow conditions have been assumed in the entire domain, i.e., not including any closure turbulence scheme.

The computational domain consisted of a conical diffuser connecting two cylindrical chambers of diameter a (Fig. 4). The throat of the cone was tapered with a fillet of radius equal to $d/2$, whereas the connection with the outlet chamber was sharp. Such inlet/outlet geometry should have favored the asymmetrical behavior of the flow in the diffuser/nozzle phases.[26] The mesh used to discretize the domain consisted of an unstructured triangular grid in the bulk region, while a structured quadrangular grid was adopted near the rigid wall (see green box in Fig. 4). The accuracy of the numerical results remained unaffected by the grid resolution, due to the utilization of over 30 000 elements (see Appendix C).

A first series of numerical experiments to evaluate the effectiveness of the theoretical solution used ten configurations of the cone with tube diameters d and D in the range from 0.1 to 10 mm, and the cone angle θ varying between $7°$ and $30°$. In all cases, the diffuser slenderness L/d was kept greater than 10. The chambers had a diameter $a = 10D$, large enough to ensure that the flow velocity was negligibly small in these portions of the domain. The numerical tests were carried out for water, hence prescribing $\rho = 1000 \, \text{kg/m}^3$ and $\nu = 1.0 \times 10^{-6} \, \text{m}^2/\text{s}$. The pressure boundary conditions were prescribed in two sections inside the chambers far from the cone (initial and final sections of the domain of Fig. 4). A sinusoidal pressure of magnitude p_0 and frequency f was imposed at the inlet, and a constant pressure equal to 0 Pa was prescribed at the outlet. Once the system reached a steady periodic state, the results of the last cycle were used in the analysis. The total runs analyzed counts 74 experiments. The studied configurations and the applied forcing conditions are summarized in Table I.

A second series of numerical simulations, aimed at investigating in detail the space of the parameters, was performed for configurations 1, 8, and 10 of the first series of tests. For these configurations, three different frequencies were considered, and for each combination configuration/frequency, the pressure p_0 was varied within a specific range of values. This series of experiments counts overall 92 runs. Details of this series of simulations are reported in Table II.

V. RESULTS AND DISCUSSION

A. Model assessment and definition of the laminar regime

We compared the time-varying flow rate $Q(t/T)$ predicted by the theoretical model and computed numerically through the CFD

TABLE I. The geometrical configurations of the duct and the characteristics of the sinusoidal forcing used in the first series of numerical experiments simulating the diffuser/nozzle pump.

Configuration	d (mm)	D (mm)	L (mm)	θ (deg)	p_0 (Pa)	f (Hz)
1	1.50	4.00	20	7.2	500–2000	1–100
2	0.75	2.00	10	7.2	1000	10–100
3	0.15	0.4	2	7.2	500–2000	1–500
4	0.75	3.25	20	7.2	500–4000	1–100
5	0.75	4.50	30	7.2	250–1000	1–100
6	0.75	3.00	10	12.8	1000	5–200
7	0.38	1.50	5	12.8	100–250	1–200
8	0.75	4.00	10	18.5	50–1000	5–200
9	0.75	5.00	10	24.0	25–1000	5–150
10	0.75	11.25	20	29.4	50–1500	5–100

18 October 2023 13:51:10

TABLE II. Geometrical configurations and characteristics of the sinusoidal forcing of the nozzle/diffuser pump simulated in the second numerical analysis.

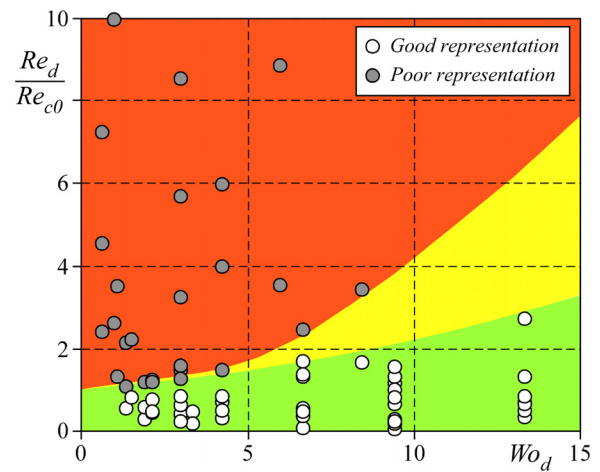| Configuration	θ (deg)	f (Hz)	p_0 (Pa)
1	7.2	10	1–500
		20	50–2000
		50	200–12 000
8	18.5	20	20–200
		50	100–1000
		200	500–12 000
10	29.4	20	20–200
		50	50–750
		100	100–3000

FIG. 6. The points representative of CFD simulations plotted in the plane $Re_d/Re_{c0} - Wo_d$ for the first series of experiments (see Table I). White circles represent numerically computed flow conditions which are well described even by Eq. (15). Gray circles represent flow conditions for which the numerical and the analytical solutions differ considerably. Green and red areas, which include the white and gray circles, respectively, indicate where the flow is expected to be laminar and dominated by inertia; the transition condition is located within the yellow area in between.

approach (Fig. 5). To fit the computed flow cycles, the parameters $\bar{\zeta}_{\pm}$, $\bar{\beta}$, and ε of Eq. (15) are assessed by a trial and error procedure. For the case with a high Strouhal number [$St = 42.6$ in Fig. 5(b)], the theoretical solutions match very well the numerical results. Interestingly, for low St, only the case shown in Fig. 5(c) ($St = 1.7$) is well predicted by Eq. (15), whereas, for $St = 0.4$ [Fig. 5(a)], some substantial differences are observed between the two solutions.

We foresee that the proposed theoretical scheme properly predicts the pump flow rate when the hydrodynamics within the diffuser/nozzle is laminar during the entire pumping cycle. As discussed in Sec. II, the oscillatory flow preserves the laminarity for higher Reynolds number, Re_d, than those observed for the steady case ($Re_d/Re_{c0} > 1$). This means that the transition between viscous loss and inertia-dominated regimes—and then the validity of the solution of Eq. (15)—is somehow controlled by the Strouhal number St.

For $St < 1$, according to Eq. (9) and recalling that $Re_{c0} = 30 L/d$, the condition of flow regime transition $Re_d/Re_{c0} = 1$, valid for steady flows, can be extended with minor approximations when Wo_d results

$$St = 4 \frac{L}{d} \frac{Wo_d^2}{Re_d} < 1 \rightarrow Wo_d \lesssim 2.7. \quad (23)$$

In addition, the linearized solution in the laminar regime is appropriate when temporal acceleration prevails over advective acceleration,[38] i.e., $St \gg 1$. With this constraint, expressed as the ratio

between the squared Womersley number and the Reynolds number, the flow is laminar as long as $Re_d \ll Re_{c0} Wo_d^2$, thus suggesting that the regime transition occurs for Reynolds numbers which scale with the squared of the Womersley number.

To define this threshold Reynolds number, Re_c, at varying working conditions, we plotted, for the series of tests reported in Table I, the points representative of CFD simulations in the plane Re_d/Re_{c0} vs Wo_d (Fig. 6) distinguishing between those for which the flow field is well or poorly described by the solution given by Eq. (15). The solution of Eq. (15) was considered to fit satisfactorily the CFD simulation, if both the differences between the theoretical and computational maximum and minimum flow rate, Q_{max} and Q_{min}, and the volumes V_+ and V_- were less than 5%.

For low values of Wo_d (i.e., $Wo_d \lesssim 3$), the condition for which $Q(t)$ given by Eq. (15) is remarkably similar to the computed one is
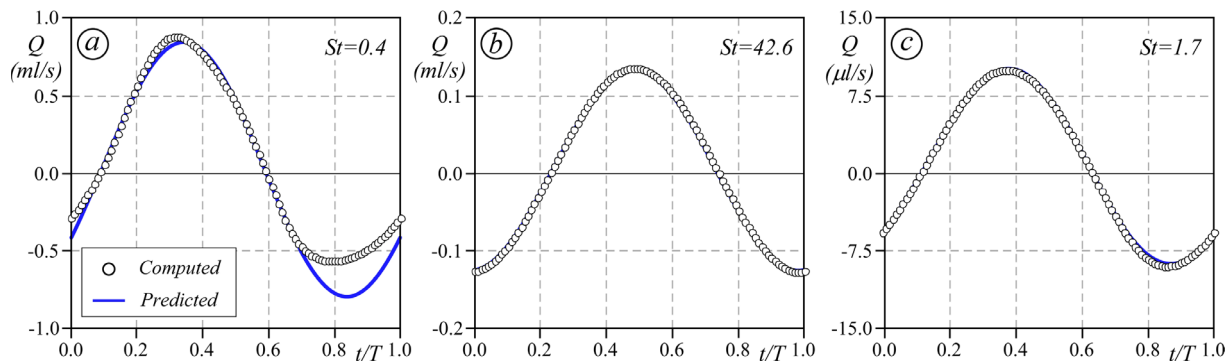

FIG. 5. Comparison between the time-varying flow rates estimated by Eq. (15) (solid blue line) and by CFD simulations (white circles) for (a) configuration 4 with $f = 10$ Hz and $p_0 = 1$ kPa, (b) configuration 4 with $f = 100$ Hz and $p_0 = 1$ kPa, and (c) configuration 3 with $f = 100$ Hz and $p_0 = 0.5$ kPa.

close to $Re_d/Re_{c0} \lesssim 1$. Hence, $Re_c = Re_{c0}$ correctly identifies the viscous/inertia-dominated regime transition. As expected, a not negligible number of numerical tests with $Re_d/Re_{c0} > 1$ are still accurately described by the laminar flow solution (i.e., those falling in the green area of Fig. 6), revealing the existence of a superlinear relationship between Re_c and Wo_d triggering to the flow transition.

According to the analysis, one argues that the transition occurs within the yellow region of Fig. 6. However, this is only the first attempt to relate the flow transition in diffuser/nozzle pipes to a Re_c for Wo_d low-moderate. Additional extensive CFD simulations and experimental tests are needed to evaluate Re_c for the diffuser/nozzle operating at moderate-high Wo_d. The analysis should also account for the cone angle since it may favor the detachment of the boundary layer when the fluid flows along the diverging wall direction. This point is supported by the CFD simulations reported in Fig. 3 that show reverse flow regions in the diffuser mode.

B. Analysis of the loss coefficients

The second series of numerical simulations allows one to study the role of advective and temporal inertia on the model parameters, i.e., the dependence of model parameters on the Reynolds and Womersley number or the ratio between the two, i.e., the Strouhal number. The determination of specific relationships to estimate the model parameters $\bar{\zeta}_{\pm}$, $\bar{\beta}$, and ε, is hardly feasible because the flow behavior depends also on other non-dimensional parameters, e.g., the cone angle and the tube slenderness. Therefore, we focus on a qualitative or semi-quantitative analysis in order to frame the peculiar characteristics of the pump dynamics and its performance in the range of the typically prescribed working conditions.[32,33] Notably, the relationships here proposed for estimating the parameters of the model with some approximation have the only purpose of showing what the dependence of these parameters on the dimensionless groups that characterize the problem is. A best-fitting approach based on a trial-and-error procedure is adopted for this aim.

In Sec. V B, we focus exclusively on the loss coefficients $\bar{\zeta}_{+}$ and $\bar{\zeta}_{-}$, which control the asymmetric flow through the pump. For readers interested, the other parameters, $\bar{\beta}$ and ε, are treated in detail in Appendix D.

The loss coefficients $\bar{\zeta}_{+}$ and $\bar{\zeta}_{-}$ estimated by comparing the solutions of Eq. (15) with those given by the CFD simulations can be approximated with the following relationships:

$$\bar{\zeta}_{+} = \left[\bar{\zeta}_0^{\lambda} + (0.15Re_d)^{\lambda}\right]^{1/\lambda} \quad , \quad \bar{\zeta}_{-} = \left[\bar{\zeta}_0^{\lambda} + 1.30\left(\frac{0.15Re_d}{\sqrt{\tan\theta}}\right)^{\lambda}\right]^{1/\lambda},$$

$$(24)$$

where λ and $\bar{\zeta}_0$ are suitable coefficients. The data analysis provides

$$\lambda = 1 + 0.0021\chi^2(\theta)Wo^{2.5},\qquad(25)$$

where $\chi(\theta)$ is a function of the cone angle, θ

$$\chi(\theta) = -0.45\ln(\tan\theta + 0.22)\qquad(26)$$

and Wo the Womersley number calculated in the middle section of the tube, $Wo = r_m\sqrt{\omega/\nu}$, with $r_m = (d + D)/4$.

In Eq. (24), the coefficient $\bar{\zeta}_0$ is the value of both $\bar{\zeta}_{+}$ and $\bar{\zeta}_{-}$ for $Re_d \ll 1$. Using the second series of experiments, $\bar{\zeta}_0$ is found to be

$$\bar{\zeta}_0 = \frac{20}{(\tan\theta)^{0.75}}\frac{d}{D} + \frac{68.5}{440^{\tan\theta}}Wo^{0.9}\qquad(27)$$

with the first term on the right-hand side directly derived from the solution for steady flow provided by Jiang *et al.*,[27] whereas the second term stems from a fitting of the numerical results. Equation (27) indicates that $\bar{\zeta}_0$ is nearly proportional to Wo, and it decreases quickly by increasing the diffuser angle, θ.

Figure 7 compares the loss coefficients $\bar{\zeta}_{+}$ [panels (a)–(c)] and $\bar{\zeta}_{-}$ [panels (d)–(f)] estimated from the numerical experiments listed in Table II with the approximate solution given by Eqs. (24)–(27). The computed $\bar{\zeta}_{\pm}$ are satisfactorily predicted, and the proposed relationships are able to catch the trend of the losses coefficients with Re_d and
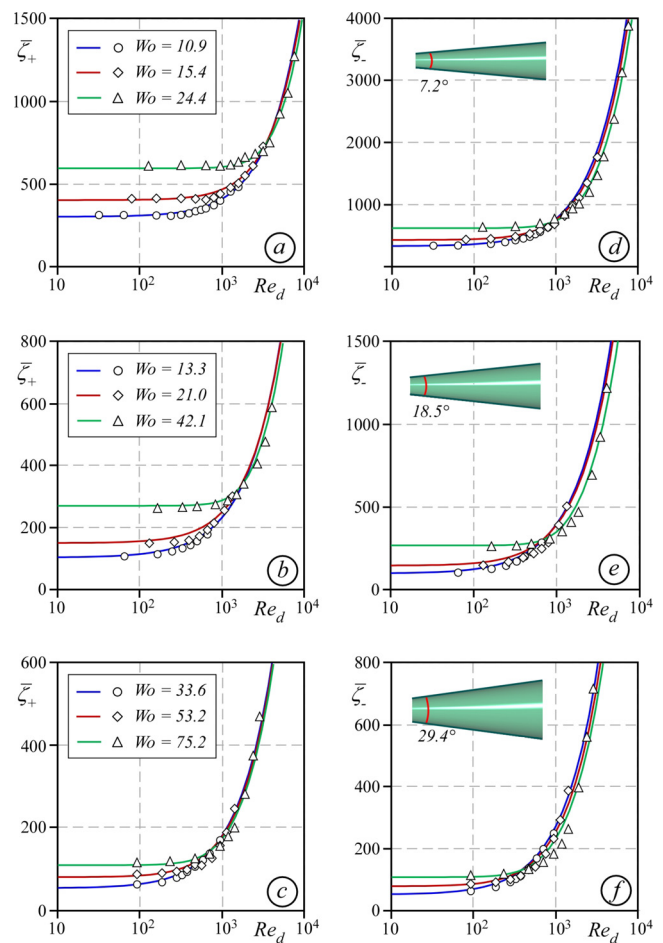

FIG. 7. Energy loss coefficients as function of Re_d for the three cone angles, θ, of Table II at different Womersley number, Wo. Panels (a)–(c) show the loss coefficient in the diffuser direction, $\bar{\zeta}_{+}$. Panels (d) and (e) show the loss coefficient in the nozzle direction, $\bar{\zeta}_{-}$. White symbols represent the values estimated when comparing CFD simulations with Eq. (15); solid colored lines the solutions predicted by Eqs. (24)–(27).
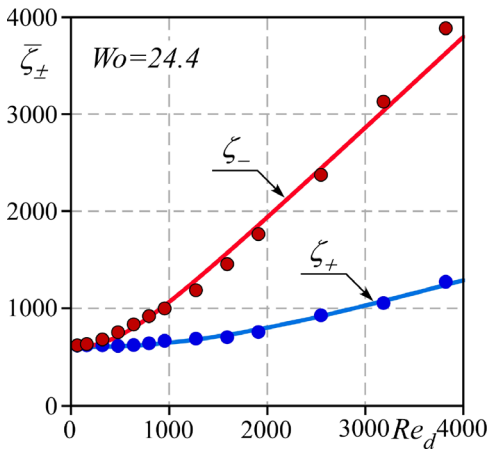
FIG. 8. Energy loss coefficient $\bar{\zeta}_+$ (blue) and $\bar{\zeta}_-$ (red) as a function of Re_d for case 1 with $f = 50$ Hz (see Table II). Circles denote the loss coefficients estimated by matching the CFD solutions with Eq. (15); solid lines show the solutions predicted by Eq. (24).

Wo varying. The losses in the nozzle flow modality largely exceed those in the diffuser case. Interestingly, the increase in Wo increases the losses when the Reynolds number is low ($Re_d < 100$) according to Eq. (27), while it slightly reduces the sharp increase in $\bar{\zeta}_\pm$ for large Re_d.

Figure 8 shows an example of how the coefficients $\bar{\zeta}_+$ and $\bar{\zeta}_-$ vary with Re_d for a given value of Wo. For $Re_d < 100$, the energy losses are weakly affected by the inertia and hence the differences between the diffuser and nozzle modality are negligibly small; on the contrary, for $Re_d > 100$, both $\bar{\zeta}_+$ and $\bar{\zeta}_-$ increase with Re_d, but $\bar{\zeta}_-$ proportionally increases less than $\bar{\zeta}_+$.

C. Pump performance

As the energy dissipation and the pump flow rate are influenced by Re_d and Wo, even the pump performance turns out to depend on these two parameters. In the scenarios analyzed, the pump efficiency is maximized when the values of the dissipation coefficients, $\bar{\zeta}_\pm$, lie along the elbow of the plots shown in Fig. 7. These maximum conditions

correspond to Reynolds numbers ranging between 500 and 3500 and increase with the Womersley number. A more effective representation of the pump's performance is possible by expressing the efficiency as a function of the Strouhal number, which can reflect the dependency of η on both the Reynolds and Womersley numbers.

Figure 9 compares the efficiency η computed using the numerical results with that estimated with the solution of Eq. (15). The latter systematically overestimates the numerical efficiency near the maximum; however, the error does not exceed 7%.

Remarkably, in some cases, the efficiency shows small negative values at high St, i.e., the average flow rate is higher in the nozzle phase than in the diffuser phase. This condition of reverse pumping may occur at low Re_d when $\bar{\zeta}_+ > \bar{\zeta}_-$.[22,39]

In the three configurations, the maximum pump performance increases with the Womersley number, Wo, whereas the overall efficiency, in the range of the investigated Wo, reduces with θ increasing. Furthermore, the optimum falls within the range $1 < St < 10$ in the three cases analyzed.

This range of St in which the efficiency is maximum is also found by the numerical analysis on the performance of a diffuser valve carried out by Wang, Chang, and Huang,[40] as well as in the experimental investigation on some micropumps reported in Wang, Chen, and Hsiao.[39]

Wang, Chen, and Hsiao carried out experiments on the rectification performance of conical diffusers. Their tests highlight an almost linear relationship between the Reynolds and Roshko number (corresponding to $Wo_d{}^2$) when the maximum flow rate in the diffuser is achieved, i.e., a condition close to that of the maximum efficiency. The diffusers tested had a cone angle that varied almost in the same range ($\theta = 10°–35°$) but with smaller slenderness than those of the present study ($L/d = 7.6$ vs 13.3). The maximum efficiency, however, resulted for St from 1.9 to 5.6, i.e., values comparable to those shown in Fig. 9.

The range $1 < St < 10$ hints at the possibility that the optimum is achieved when the convective and temporal inertia balance. Consequently, such Strohual interval should be the natural operating condition of circulation that exploits diffuser/nozzle pumps.

Longatti et al.,[7] based on the analysis of magnetic resonance images of a cohort of ten voluntaries, proposed a simplified diffuser/nozzle pump model to describe the cerebrospinal pulsatile flow (CSF)
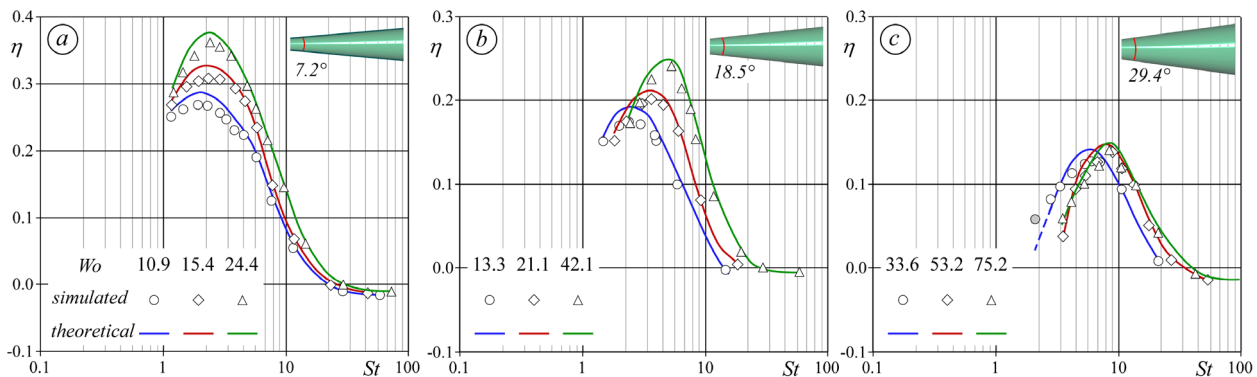

FIG. 9. Pump efficiency, η, as a function of St for (a) configuration 1 ($\theta = 7.2°$), (b) configuration 4 ($\theta = 18.5°$), and (c) configuration 8 ($\theta = 29.4°$). The white symbols are the values computed from the CFD simulations at different Wo; solid colored lines those predicted from the solution given by Eq. (15). The gray circle in panel (c) denotes the solution computed in the presumed inertia-dominated flow regime.

through the system composed of the Third ventricle, the Sylvius aqueduct, and the Fourth ventricle. In the model, the anatomy of the aqueduct connecting the two ventricular chambers is described as a short straight tube of length $l = 17$ mm and diameter $d_0 = 1.6$ mm followed by a tapered diffuser of length $L = 13$ mm with the smallest and largest diameter equal to $d = d_0 = 1.6$ and $D = 4.5$ mm (the cone angle is thus $\theta = 12.7°$). Although the geometry is not a standard tapered diffuser/nozzle, the flow still experiences different resistances in the two directions similarly to the present model of the valveless pump. The liquor in the CSF circulation has the same characteristics as water ($\rho \cong 1000$ kg/m^3 and $\nu \cong 10^{-6}$ m^2/s). The fluid is mainly pumped by the external pressure due to the heartbeat (frequency $f \cong 1$ Hz), resulting in an oscillatory discharge through the aqueduct whose peak lays in the range $Q_0 = 10$–20 ml/min.[41–43] With these data, the estimate of the Strouhal number of the Sylvius aqueduct is $St = 1.1$–2.3.

The above result shows that the third ventricle-sylvius aqueduct-fourth ventricle system, modeled as a valveless pump, operates under the expected conditions of maximum efficiency. Interestingly, the physiological microcirculation in organisms generally occurs with pulsatility ω of order 10 Hz and p_0 between 100 and 1000 Pa. In the present analysis, $\bar{\zeta}$ is shown to be of the order 100–1000 according to Eq. (24), and therefore St turns out to be of order 1, according to Eq. (22).

These noteworthy results seem to confirm that $St = 1$–10 is probably the typical range of the Strouhal number in micropumps adopted for microcirculation in nature. Clearly, the problem at hand is extremely complex and further specific investigations are necessary to confirm the significance of the outcomes given by the present simplified model.

Finally, Fig. 10 shows the normalized net flux Q_{net}/Q_0 as a function of St for configuration 1. The comparison between panel (a) of Figs. 9 and 10 shows that the net flow rate, $Q_{net} = \varepsilon Q_0 \Delta\bar{\zeta}/\bar{\zeta}$, has the same trend as η, and, in particular, the maximum of the ratio $\frac{Q_{net}}{Q_0}$ occurs approximately at the same St that characterizes the maximum pump efficiency.
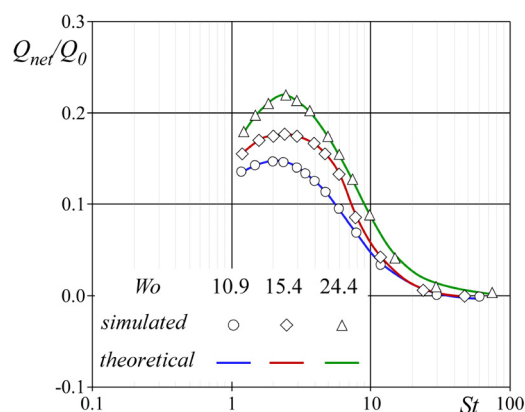

FIG. 10. Q_{net}/Q_0 as a function of St for configuration 1 ($\theta = 7.2°$) at three different Wo (see Table II). White symbols are the values computed from the CFD simulations at different Wo; solid colored lines are those predicted from the solution given by Eq. (15).

VI. CONCLUSIONS

An approximate time-dependent theoretical solution based on the mechanical energy conservation equation is proposed to predict the laminar flow rate through an ideal diffuser/nozzle pump. When the flow is laminar, the solution matches the results of numerical simulations carried out using several diffuser/nozzle configurations. Interestingly, when the temporal inertia is relatively large, the onset of the transition from laminar to inertia-dominated flow shifts toward higher values of the Reynolds number. A transition criterion is also proposed, i.e., the transition occurs when the Reynolds number, Re_d, exceeds a threshold value Re_c, which in turn depends on the throat Womersley number, Wo_d.

The correct predictions of the proposed solution depend on four parameters, namely $\bar{\zeta}_\pm$, $\bar{\beta}$, and ε. Despite the large number of numerical experiments performed, the characterization of these parameters was not complete in the space of the non-dimensional groups that govern the dynamics (Re, Wo, St, L/d, and θ). This aspect, thus, deserves further studies to fully explore the problem and use the simplified 1D solution straightforwardly. However, the analysis points out some relevant results.

The pump efficiency decreases dramatically with the cone angle θ increasing in the three cases analyzed and depends on the competition between viscosity and advective and temporal inertia, described by the dimensionless parameters Re_d, Wo, and St. The optimal valveless pump function is achieved for $St = O(1)$ when the advective and temporal inertia are balanced. This condition is also observed in natural channels, as in the cerebrospinal circulation, in which the Sylvius aqueduct appears to function as a diffuser/nozzle element.

Furthermore, the efficiency is mainly controlled by the loss coefficients $\bar{\zeta}_\pm$, which, in turn, depend on Re_d, Wo, and the geometry of the diffuser/nozzle. Specifically, the loss coefficients, $\bar{\zeta}_\pm$, growth with Re_d, but result strongly dependent on the Womersley number, Wo, for $Re_d < 100$.

Based on the assumptions of incompressible Newtonian fluid, the model is suitable for water and organic solvents; on the contrary, some cautions are needed to apply the present scheme to fluids with low bulk modulus, such as air or gas, or different rheology, such as blood and industrial oils. That being said, gases can be treated as incompressible in diffuser/nozzle pumps that operate under the flow rates used in the current study, whereas the non-Newtonian behavior can be appropriately included in the energy losses.

A more accurate estimation of the loss coefficients at different operating conditions is a challenging problem that needs to be dealt with to enhance the comprehension of this intriguing hydraulic mechanism, with positive benefits in the design of asymmetric micropumps, as well as in the understanding of the dynamic conditions that may favor asymmetric pumping systems in biological flows at small scales.

AUTHOR DECLARATIONS
Conflict of Interest

The author has no conflicts to disclose.

Author Contributions

Paolo Peruzzo: Conceptualization (equal); Data curation (equal); Formal analysis (equal); Investigation (equal); Methodology (equal); Software (equal); Validation (equal); Writing – original draft (equal).

DATA AVAILABILITY

The data that support the findings of this study are openly available in *Data of numerical simulations on micropumps* at http://researchdata.cab.unipd.it/id/eprint/572, DOI *10.25430/researchdata.cab.unipd.it.00000541*.

NOMENCLATURE

a	chamber radius
A	section area
$A1, A2$	section area of the chamber 1 and 2
C	constant of integration
d	throat diffuser/nozzle diameter
D	maximum diffuser/nozzle diameter
f	pumping frequency
g	gravity acceleration
H	total head
j	head loss per unit length
L	diffuser/nozzle length
$\mathbf{n}$	normal vector
p	pressure
p_{max}	maximum efficiency pressure
p_0	maximum pressure difference between chambers 1 and 2
p_1, p_2	pressure in chamber 1 and 2
Q	volumetric flow rate
Q_{net}	net flow rate
Q_0	characteristic flow rate
r	radial direction
Re_c	critical Reynolds number
Re_{c0}	critical Reynolds number in steady flow
Re_d	throat Reynolds number
s	axial direction
St	Strouhal number
t	time
T	pumping period
$\mathbf{T}$	tensor stress
$\mathbf{u}$	local flow velocity
u	axial flow velocity
U	cross-sectional average velocity
U_0	characteristic flow velocity
v	radial flow velocity
V	domain volume
V_+	total volume flowing in the diffuser mode
V_-	total volume flowing in the nozzle mode
Wo	Womersley number in the middle of the diffuser/nozzle
Wo_d	throat Womersley number
α	Coriolis correction factor
β	momentum-flux correction factor
β_m	median of the momentum-flux correction factor

$\bar{\beta}$	time-independent momentum-flux correction factor
$\bar{\beta}_\infty$	asymptotic momentum-flux correction factor
γ	fluid specific gravity
$\Delta\bar{\zeta}$	semi-difference of the time-independent Energy loss coefficients
$\Delta\Pi_{1,2}$	power of the internal forces
$\Delta\psi$	semi-difference of the characteristic frequencies
ε	calibration factor
ζ	energy loss coefficient
$\bar{\zeta}$	averaged time-independent Energy loss coefficient
$\bar{\zeta}_0$	energy loss coefficient at $Re_d \ll 1$
ζ_+	energy loss coefficient in the diffuser mode
ζ_-	energy loss coefficient in the nozzle mode
$\bar{\zeta}_+$	time-independent energy loss coefficient in the diffuser mode
$\bar{\zeta}_-$	time-independent energy loss coefficient in the nozzle mode
η	kinematic viscosity
η	pump efficiency
θ	cone angle
κ	coefficient
λ	coefficient
μ	dynamic viscosity
ρ	fluid density
$\sigma = \psi/\omega$	frequencies ratio
$\chi(\theta)$	function of the cone angle θ
ψ	diffuser/nozzle characteristic frequency
ψ_+, ψ_-	characteristic frequencies of the diffuser (subscript $+$) and nozzle mode (subscript $-$)
ω	pumping angular frequency
ω_{max}	maximum efficiency pulsatility
Ω	surface boundary
$\tilde{}$	dimensionless parameter

APPENDIX A: DERIVATION OF THE MECHANICAL ENERGY CONSERVATION IN A DIFFUSER/NOZZLE ELEMENT

The pump dynamics can be described by assuming the mechanical energy conservation for an uncompressible flow of density ρ on the control volume, V, limited by the surface Ω, which reads

$$\frac{d}{dt}\underbrace{\int_V \rho\frac{u^2+v^2}{2}dV}_{kinetic\ energy} + \underbrace{\int_\Omega \mathbf{u}\cdot(\mathbf{T}\cdot\mathbf{n})\,d\Omega}_{power\ of\ external\ forces} + \underbrace{\Delta\Pi_{1,2}}_{power\ of\ internal\ forces} = 0,$$

(A1)

where u and v are the axial (direction s) and radial (direction r) components of the local velocity $\mathbf{u}$, respectively, $\mathbf{T}$ is the tensor stress, and $\Delta\Pi_{1,2}$ is total power dissipated within V. The first integral accounts for the variation of the kinetic energy in V; the second is instead the power of the external forces owing to the pressure and the shear stress on the boundaries ($\mathbf{n}$ is the normal vector directed outwardly from Ω). However, at the wall, the velocity is $\mathbf{u} = 0$ (no-slip condition); therefore, the contribution of $\mathbf{T}$ is null, and the power depends only on the pressure, p, acting on the inlet and outlet of the domain. Accordingly, we can rearrange Eq. (A1), as

$$\int_V \rho \frac{d}{dt}\left(\frac{u^2 + v^2}{2}\right) dV \approx \frac{\rho}{2}\int_V \frac{\partial u^2}{\partial t} dV + \frac{\rho}{2}\int_V \left(u\frac{\partial u^2}{\partial s} + v\frac{\partial u^2}{\partial r}\right) dV$$

$$= -\int_{A_2} p\, u\, dA + \int_{A_1} p\, u\, dA - \Delta\Pi_{1,2}, \quad \text{(A2)}$$

here the kinetic energy contribution is approximated to $\rho\, u^2/2$ since $v \ll u$, and A_1 and A_2 are the inlet and outlet sections where $\mathbf{u} = (u, 0)$ and p is constant. The integrals of Eq. (A2) can be solved in terms of the cross-sectionally averaged velocity, U, by introducing the correction factors

$$\alpha = \frac{1}{A}\int_A \frac{u^3}{U^3} dA, \quad \beta = \frac{1}{A}\int_A \frac{u^2}{U^2} dA. \quad \text{(A3)}$$

By replacing these terms in Eq. (A2) and observing that the integral of $v\partial u^2/\partial r$ is zero owing to the axial symmetry of the problem, we find

$$\left(p_2 + \rho\alpha_2 U_2^2\right) - \left(p_1 + \rho\alpha_1 U_1^2\right) = -\rho\int_1^2 \beta\frac{\partial U}{\partial t} ds - \frac{\Delta\Pi_{1,2}}{Q}, \quad \text{(A4)}$$

where $Q = U\,A$ is the volume flow rate through the pipe. Here, the first and second terms are the mechanical energy per unit volume of fluid in the outlet and inlet, respectively, while the third term is the temporal variation of the energy. Finally, by dividing by the specific gravity of the fluid, γ, the differentiation of Eq. (A4) results in Eq. (2).

APPENDIX B: DERIVATION OF THE FLOW RATE DIFFERENTIAL EQUATION

The volume flux, Q, is determined by integrating Eq. (2) between the two chambers, i.e.,

$$\int_1^2 \frac{\partial H(s,t)}{\partial s} ds = -\int_1^2 \frac{\beta(s,t)}{g}\frac{\partial U(s,t)}{\partial t} ds - \int_1^2 j(s,t)\, ds. \quad \text{(B1)}$$

The integral on the left-hand side of Eq. (B1) yields the total head difference $H_2(t) - H_1(t)$, which is equal to the difference in pressure $p_2(t)/\gamma - p_1(t)/\gamma$, as the flow velocity is negligibly small in the chambers, that is,

$$\int_1^2 \frac{\partial H(s,t)}{\partial s} ds = \frac{p_2(t)}{\gamma} - \frac{p_1(t)}{\gamma} = \frac{p_0}{\gamma}\sin(\omega t). \quad \text{(B2)}$$

The term $\partial U/\partial t$ is also negligible within the two chambers, and the first term on the right-hand side can be rewritten as

$$-\frac{1}{g}\int_1^2 \beta\left(\frac{1}{A}\frac{\partial Q}{\partial t} - \frac{Q}{A^2}\frac{\partial A}{\partial t}\right) ds, \quad \text{(B3)}$$

where $A = A(s,t)$ is the cross section area of the nozzle. Furthermore, being fluid incompressible and the wall rigid, Eq. (B3) can be simplified as follows:

$$-\frac{1}{g}\int_1^2 \beta\left(\frac{1}{A}\frac{\partial Q}{\partial t} - \frac{Q}{A^2}\frac{\partial A}{\partial t}\right) ds = -\frac{1}{g}\frac{dQ}{dt}\int_1^2 \frac{\beta}{A} ds. \quad \text{(B4)}$$

Referring to Fig. 2(a), the cross-sectional area $A(s)$ reads

$$A(s) = \frac{\pi}{4}d(s)^2 = \frac{\pi}{4}\left(d + 2\frac{D-d}{2L}s\right)^2 = \frac{\pi}{4}(d + 2\tan\theta s)^2. \quad \text{(B5)}$$

Substituting (B5) in (B4) and assuming self-similar velocity profiles along the pipe, such that $\beta(s,t) \approx \beta(t)$, integration by parts leads to

$$\int_1^2 \frac{\beta}{A} ds = \frac{4}{\pi}\int_1^2 \frac{\beta}{(d + 2\tan\theta s)^2} ds$$

$$= \frac{4\beta}{2\tan\theta\pi}\int_d^D \frac{1}{\xi^2} d\xi$$

$$= -\frac{4L\beta}{(D-d)\pi}\left(\frac{1}{D} - \frac{1}{d}\right) = \frac{4L\beta}{\pi dD}. \quad \text{(B6)}$$

By substituting (B4) and (B6) into (B3), the inertial acceleration can be rewritten as

$$-\frac{1}{g}\int_1^2 \frac{\partial Q}{\partial t}\frac{\beta}{A} ds = -\frac{\beta}{g}\frac{4L}{\pi dD}\frac{dQ}{dt}. \quad \text{(B7)}$$

The overall energy loss, quantified by the last integral of the right-hand side of Eq. (B1), can be estimated by means of semiempirical relations valid for laminar flow condition, e.g., Jiang *et al.*[27]

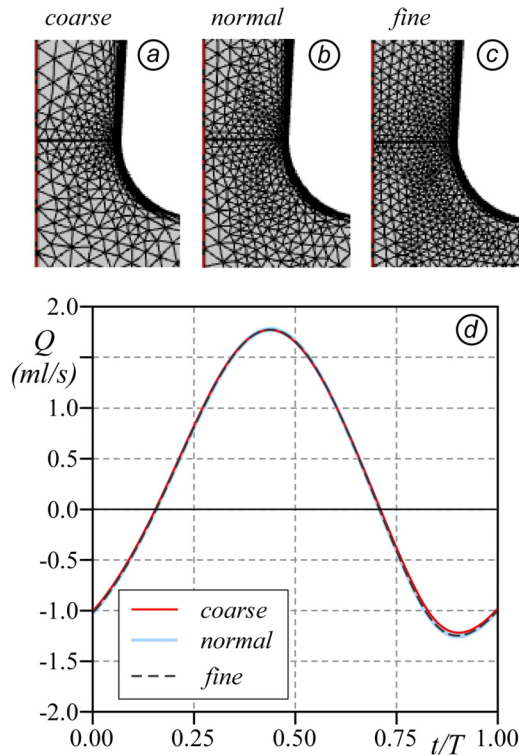$$-\int_1^2 j\, ds = -\frac{\zeta(t)}{g}\frac{2\nu}{\pi d^3}Q(t). \quad \text{(B8)}$$

FIG. 11. Sensitivity analysis of the grid resolution. Panels (a)–(c) show the coarse mesh (5400 elements), the normal mesh (32 000 elements), and the fine mesh (115 000 elements) adopted in the simulation. Panel (d) shows the computed flow rates for configuration 1 by prescribing $f = 10$ Hz and $p_0 = 500$ Pa with the coarse (solid red line), normal (solid sky blue line), and fine (dashed dark gray line) mesh.

APPENDIX C: MESH SENSITIVITY ANALYSIS

To test the influence of the grid resolution on the results, we compared the flow rate computed for configuration 1 using three meshes that consist indicatively of 5400 (coarse), 32 000 (normal), and 115 000 (fine) elements (see Fig. 11).

The values of the three flow rates are similar. Relative errors between the solutions with the normal and coarse mesh are below 3%, while between the normal and fine mesh are smaller than 0.3%.

APPENDIX D: ANALYSIS OF $\bar{\beta}$ AND ε

1. The momentum correction factor $\bar{\beta}$

As an example, Fig. 12 shows the values of $\bar{\beta}$ for configuration 1 of the second series of simulations (see Table II) as a function of the Strouhal number, St. For each Wo, $\bar{\beta}$ increases with St, and it approaches a constant value as soon as St is sufficiently large ($St \to \infty$); we denote such a asymptotic value by $\bar{\beta}_{\infty}$.
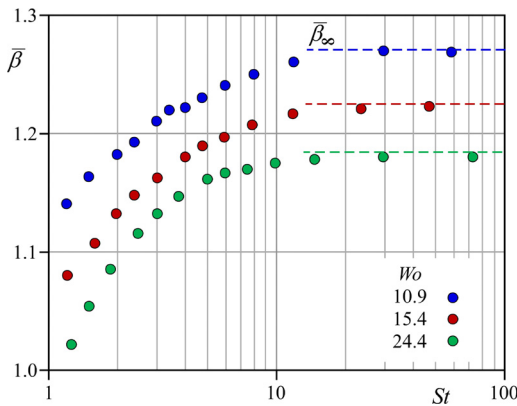

FIG. 12. The momentum corrector factor, $\bar{\beta}$, vs St for configuration 1 (see Table II). Circles denote the estimates of $\bar{\beta}$ given by matching the CFD solutions with Eq. (15) with Wo equal to 10.9 (blue), 15.4 (red), and 24.4 (green). The dashed lines represent the asymptote $\bar{\beta}_{\infty}$ for the three series of data.
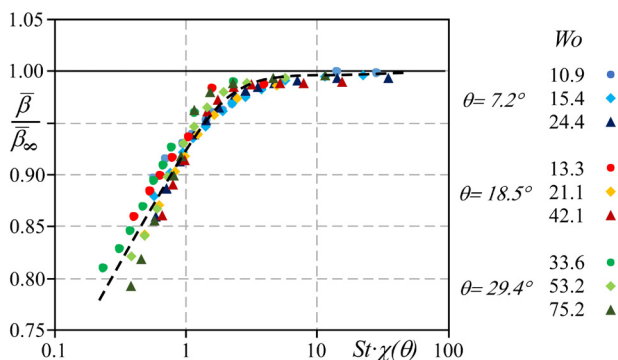

FIG. 13. Estimated $\bar{\beta}/\bar{\beta}_{\infty}$ vs $St \cdot \chi(\theta)$ for the second series of experiments distinguished for Wo (see Table II). Blue symbols refer to configuration 1 ($\theta = 7.2°$), red symbols to configuration 4 ($\theta = 18.5°$), and green symbols to configuration 8 ($\theta = 29.4°$). The dashed line shows the trend of the overall data.
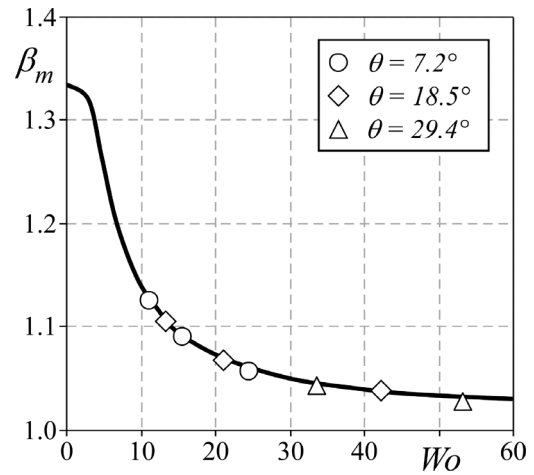

FIG. 14. The median of the momentum correction factor, β_m, as a function of Wo, computed at the highest St for each frequency of the second series of experiments (see the test with smallest p_0 in Table II). Circles refer to configuration 1 ($\theta = 7.2°$), diamonds to configuration 4 ($\theta = 18.5°$), and triangles to configuration 8 ($\theta = 29.4°$). The results are satisfactorily located on the solid line indicating β_m calculated according to the solution of pulsatile flow in a straight tube.[44]

The most striking result is shown in Fig. 13 where the ratio $\bar{\beta}/\bar{\beta}_{\infty}$ is plotted vs $St \cdot \chi(\theta)$ for the three configurations analyzed. The data lie with minor scatter along the black dashed line, indicating that $\chi(\theta)$ and $\bar{\beta}_{\infty}$ account for the major effects of the cone angle.

The asymptotic $\bar{\beta}_{\infty}$ results to be well predicted by the following expression:

$$\bar{\beta}_{\infty} = \left[(1.07 + 0.68 \tan \theta) Wo^{-0.09 \tan \theta}\right] \beta_m, \qquad \text{(D1)}$$

where β_m is the median of the momentum correction factor in the middle tube section during the period T, when the advective velocity is neglected according to the flow solution proposed by Womersley[44] for the case of a rigid circular pipe under sinusoidal pressure gradient (see Fig. 14).
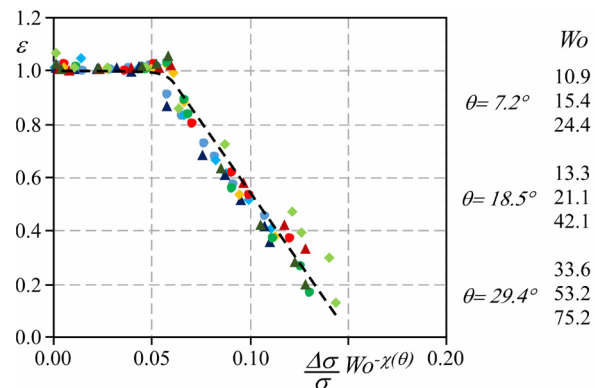

FIG. 15. Estimated ε vs $Wo^{-\chi(\theta)} \Delta\sigma/\sigma$ for the second series of experiments distinguished for Wo (see Table II). Blue symbols refer to configuration 1 ($\theta = 7.2°$), red symbols to configuration 4 ($\theta = 18.5°$), and green symbols to configuration 8 ($\theta = 29.4°$). The dashed line shows the trend of the overall data.

18 October 2023 13:51:10

The term in the square brackets of Eq. (D1) embodies the cone effect on the value of $\bar{\beta}_\infty$ (and $\bar{\beta}$); when the tube is straight, that is, when $\theta = 0$, the term in the square brackets is equal to 1.07, that is not much different from 1, as one would expect in this case.

2. The flow rate correction factor ε

Figure 15 shows the coefficient ε as it varies with $Wo^{-\chi(\theta)}\Delta\sigma/\sigma$. When $\Delta\sigma/\sigma < 0.06Wo^{\chi(\theta)}$, the flow rate correction factor ε is constant and approximately equal to one; for $Wo^{-\chi(\theta)}\Delta\sigma/\sigma > 0.06$, ε reduces linearly within the range of the investigated flow and geometry conditions.

REFERENCES

[1]P. Gravesen, J. Branebjerg, and O. S. Jensen, "Microfluidics—A review," J. Micromech. Microeng. **3**, 168 (1993).

[2]Q. Cui, C. Liu, and X. F. Zha, "Study on a piezoelectric micropump for the controlled drug delivery system," Microfluid. Nanofluid. **3**, 377–390 (2007).

[3]K. Junwu, Y. Zhigang, P. Taijiang, C. Guangming, and W. Boda, "Design and test of a high-performance piezoelectric micropump for drug delivery," Sens. Actuators, A **121**, 156–161 (2005).

[4]S. Cheng, K. Tan, and L. E. Bilston, "The effects of the interthalamic adhesion position on cerebrospinal fluid dynamics in the cerebral ventricles," J. Biomech. **43**, 579–582 (2010).

[5]A. S. Forouhar, M. Liebling, A. Hickerson, A. Nasiraei-Moghaddam, H.-J. Tsai, J. R. Hove, S. E. Fraser, M. E. Dickinson, and M. Gharib, "The embryonic vertebrate heart tube is a dynamic suction pump," Science **312**, 751–753 (2006).

[6]Z. Li, Y. Seo, O. Aydin, M. Elhebeary, R. D. Kamm, H. Kong, and M. T. A. Saif, "Biohybrid valveless pump-bot powered by engineered skeletal muscle," Proc. Natl. Acad. Sci. **116**, 1543–1548 (2019).

[7]P. Longatti, A. Fiorindi, P. Peruzzo, L. Basaldella, and F. M. Susin, "Form follows function: Estimation of CSF flow in the third ventricle–aqueduct–fourth ventricle complex modeled as a diffuser/nozzle pump," J. Neurosurg. **133**, 894–901 (2019).

[8]J. Männer, A. Wessel, and T. M. Yelbuz, "How does the tubular embryonic heart work? looking for the physical mechanism generating unidirectional blood flow in the valveless embryonic heart tube," Dev. Dyn. **239**, 1035–1046 (2010).

[9]A. Santhanakrishnan and L. A. Miller, "Fluid dynamics of heart development," Cell Biochem. Biophys. **61**, 1–22 (2011).

[10]S. Sincomb, W. Coenen, A. Sánchez, and J. Lasheras, "A model for the oscillatory flow in the cerebral aqueduct," J. Fluid Mech. **899**, R1 (2020).

[11]X. Miao, H. Lu, H. Chen, and S. Liu, "Design and research of the one-way microsphere valve and the PDMS film electromagnetic micropump," Microfluid. Nanofluid. **26**, 67 (2022).

[12]A. Borzi and G. Propst, "Numerical investigation of the liebau phenomenon," Z. Angew. Math. Phys. **54**, 1050–1072 (2003).

[13]A. I. Hickerson, D. Rinderknecht, and M. Gharib, "Experimental study of the behavior of a valveless impedance pump," Exp. Fluids **38**, 534–540 (2005).

[14]P. Longatti, "The liebau phenomenon: A translational approach to new paradigms of CSF circulation and related flow disturbances," Child's Nervous Syst. **34**, 227–233 (2018).

[15]G. Amselem, C. Clanet, and M. Benzaquen, "Valveless pumping at low Reynolds numbers," Phys. Rev. Appl. **19**, 024017 (2023).

[16]A. Olsson, G. Stemme, and E. Stemme, "Simulation studies of diffuser and nozzle elements for valve-less micropumps," in *Proceedings of International Solid State Sensors and Actuators Conference (Transducers' 97)* (IEEE, 1997), Vol. 2, pp. 1039–1042.

[17]E. Stemme and G. Stemme, "A valveless diffuser/nozzle-based fluid pump," Sens. Actuators, A **39**, 159–167 (1993).

[18]M. Majhi, A. Nayak, and S. Sahoo, "Effects of hydrophobic slips in non-uniform electrokinetic transport of charged viscous fluid in nozzle-diffuser," Phys. Fluids **35**, 012014 (2023).

[19]T. Gerlach and H. Wurmus, "Working principle and performance of the dynamic micropump," Sens. Actuators, A **50**, 135–140 (1995).

[20]A. Ullmann and Y. Taitel, "The piezoelectric valve-less pump: Series and parallel connections," J. Fluids Eng. **137**, 021104 (2015).

[21]R. R. Gidde, P. M. Pawar, B. P. Ronge, and V. P. Dhamgaye, "Design optimization of an electromagnetic actuation based valveless micropump for drug delivery application," Microsyst. Technol. **25**, 509–519 (2019).

[22]V. Singhal, S. V. Garimella, and J. Y. Murthy, "Low Reynolds number flow through nozzle-diffuser elements in valveless micropumps," Sens. Actuators, A **113**, 226–235 (2004).

[23]C. Sun and K. Huang, "Numerical characterization of the flow rectification of dynamic microdiffusers," J. Micromech. Microeng. **16**, 1331 (2006).

[24]K.-S. Yang, T.-F. Chao, I. Y. Chen, C.-C. Wang, and J.-C. Shyu, "A comparative study of nozzle/diffuser micropumps with novel valves," Molecules **17**, 2178–2187 (2012).

[25]Y.-H. Xu, W,-P. Yan, K.-R. Qin, and T. Cao, "Three-dimensional flow field simulation of steady flow in the serrated diffusers and nozzles of valveless micro-pumps," J. Hydrodyn. **31**, 413–420 (2019).

[26]A. Olsson, G. Stemme, and E. Stemme, "Numerical and experimental studies of flat-walled diffuser elements for valve-less micropumps," Sens. Actuators, A **84**, 165–175 (2000).

[27]X. Jiang, Z. Zhou, X. Huang, Y. Li, Y. Yang, and C. Liu, "Micronozzle/diffuser flow and its application in micro valveless pumps," Sens. Actuators, A **70**, 81–87 (1998).

[28]A. Olsson and E. Stemme *et al.*, "Diffuser-element design investigation for valve-less pumps," Sens. Actuators, A **57**, 137–143 (1996).

[29]L. Pan, T. Ng, X. Wu, and H. Lee, "Analysis of valveless micropumps with inertial effects," J. Micromech. Microeng. **13**, 390 (2003).

[30]L. Pan, T. Ng, G. Liu, K. Lam, and T. Jiang, "Analytical solutions for the dynamic analysis of a valveless micropump—A fluid–membrane coupling study," Sens. Actuators, A **93**, 173–181 (2001).

[31]S. Singh, N. Kumar, D. George, and A. Sen, "Analytical modeling, simulations and experimental studies of a PZT actuated planar valveless PDMS micropump," Sens. Actuators, A **225**, 81–94 (2015).

[32]C. Jenke, S. Kager, M. Richter, and C. Kutter, "Flow rate influencing effects of micropumps," Sens. Actuators, A **276**, 335–345 (2018).

[33]A. Olsson, G. Stemme, and E. Stemme, "A numerical design study of the valveless diffuser pump using a lumped-mass model," J. Micromech. Microeng. **9**, 34 (1999).

[34]I. Eames, A. Azarbadegan, and M. Zangeneh, "Analytical model of valveless micropumps," J. Microelectromech. Syst. **18**, 878–883 (2009).

[35]R. Fox and S. Kline, "Flow regimes in curved subsonic diffusers," J. Fluids Eng. **84**, 303–312 (1962).

[36]O. J. Lobo and D. Chatterjee, "Development of flow in a square mini-channel: Effect of flow oscillation," Phys. Fluids **30**, 042003 (2018).

[37]M. Ohmi and M. Iguchi, "Critical Reynolds number in an oscillating pipe flow," Bull. JSME **25**, 165–172 (1982).

[38]C. K. Batchelor and G. Batchelor, *An Introduction to Fluid Dynamics* (Cambridge University Press, 2000).

[39]Y.-C. Wang, H.-Y. Chen, and Y.-Y. Hsiao, "Experimental study of the flow rectification performance of conical diffuser valves," Acta Mech. **219**, 15–27 (2011).

[40]C.-T. Wang, P.-C. Chang, and C.-C. Huang, "Optimization of diffuser valves," J. Mar. Sci. Technol. **16**, 134–138 (2008).

[41]V. Kurtcuoglu, M. Soellinger, P. Summers, K. Boomsma, D. Poulikakos, P. Boesiger, and Y. Ventikos, "Computational investigation of subject-specific cerebrospinal fluid flow in the third ventricle and aqueduct of sylvius," J. Biomech. **40**, 1235–1245 (2007).

[42]M. E. Wagshul, J. J. Chen, M. R. Egnor, E. J. McCormack, and P. E. Roche, "Amplitude and phase of cerebrospinal fluid pulsations: Experimental studies and review of the literature," J. Neurosurg. **104**, 810–819 (2006).

[43]M. E. Wagshul, P. K. Eide, and J. R. Madsen, "The pulsating brain: A review of experimental and clinical studies of intracranial pulsatility," Fluids Barriers CNS **8**, 5 (2011).

[44]J. R. Womersley, "Method for the calculation of velocity, rate of flow and viscous drag in arteries when the pressure gradient is known," J. Physiol. **127**, 553–563 (1955).

18 October 2023 13:51:10